

Periodic array of Bose-Einstein condensates in a magnetic lattice

S. Jose,¹ P. Surendran,¹ Y. Wang,¹ I. Herrera,¹ L. Krzemien,² S. Whitlock,³ R. McLean,¹ A. Sidorov,¹ and P. Hannaford^{1,*}

¹Centre for Quantum and Optical Science, Swinburne University of Technology, Melbourne 3122, Australia

²Jerzy Haber Institute of Catalysis and Surface Chemistry, Polish Academy of Sciences, 30-239 Krakow, Poland

³Physikalisches Institut, Universität Heidelberg, Im Neuenheimer Feld 226, 69120 Heidelberg, Germany

(Received 11 December 2013; published 14 May 2014)

We report the realization of a periodic array of Bose-Einstein condensates (BECs) of ^{87}Rb $F = 1$ atoms trapped in a one-dimensional magnetic lattice close to the surface of an atom chip. A clear signature for the onset of BEC in the magnetic lattice is provided by *in situ* site-resolved radio-frequency spectra, which exhibit a pronounced bimodal distribution consisting of a narrow component characteristic of a BEC together with a broad thermal cloud component. Similar bimodal distributions are found for various sites across the magnetic lattice. The realization of a periodic array of BECs in a magnetic lattice represents a major step towards the implementation of magnetic lattices for quantum simulation of many-body condensed matter phenomena in lattices of complex geometry and arbitrary period.

DOI: [10.1103/PhysRevA.89.051602](https://doi.org/10.1103/PhysRevA.89.051602)

PACS number(s): 67.85.Hj, 37.10.Gh, 37.10.Jk, 67.10.Ba

Optical lattices based on arrays of optical dipole traps are used extensively to trap periodic arrays of ultracold atoms and quantum degenerate gases in a broad range of applications. These range from simulations of condensed matter phenomena [1] to studies of low-dimensional quantum gases [2], high precision atomic clocks [3], and registers for quantum information processing [4,5]. A potentially powerful alternative approach involves magnetic lattices based on periodic arrays of magnetic microtraps created by permanent magnetic microstructures [6–16], current-carrying wires [17–19], or vortex arrays in superconducting films [20]. Magnetic lattices based on patterned magnetic films may, in principle, be tailored to produce two-dimensional (2D) [or one-dimensional (1D)] arrays of atomic ensembles in arbitrary configurations [12]. Periodicities may range from tens of micrometers, i.e., the interesting range for Rydberg-interacting quantum systems, such as Rydberg-dressed Bose-Einstein condensates (BECs) [21] and Rydberg-mediated quantum gates [15,22], down to below the optical wavelength where tunneling coupling strengths may exceed those possible with conventional optical lattices. Currently, there is also much interest in creating 2D periodic lattices of complex geometry, such as triangular, honeycomb, kagome, and superlattices, in order to simulate condensed matter phenomena [23], including exotic quantum phases, such as graphene-like states [24–26], which are predicted to occur in lattices with noncubic symmetry.

Despite these prospects for magnetic lattices, little has been achieved to date, compared to optical lattices, in part due to the difficulty in controlling the resulting potentials, including magnetic homogeneity and efficient loading of the microtraps. Another serious challenge is to overcome the inelastic collision losses which can occur at high atom densities and which are accentuated when miniaturizing the traps. For example, previous experiments involving 2D arrays of magnetic microtraps with a period of about $25\ \mu\text{m}$ [11] were limited by rapid three-body loss (decay rates $>20\ \text{s}^{-1}$) which

precluded the formation of Bose-Einstein condensates with observable condensate fractions.

In this Rapid Communication we report clear signatures for the realization of a periodic array of BECs of ^{87}Rb atoms in a 1D $10\text{-}\mu\text{m}$ -period magnetic lattice. The signature for the onset of BEC is provided by *in situ* site-resolved radio-frequency (rf) spectroscopy [11,27]. To minimize three-body losses in the magnetic lattice the atoms are prepared in the $|F = 1, m_F = -1\rangle$ low-field seeking state which has a three-times smaller three-body recombination coefficient [28,29] and weaker magnetic confinement than the $|F = 2, m_F = +2\rangle$ state on which previous work was based [11]. Additionally, we employ lattice traps with lower trap frequencies and hence lower peak atom densities. The realization of a periodic array of BECs in a magnetic lattice represents a major step towards creating periodic arrays of BECs in more complex lattice geometries with smaller lattice periods which are required for simulation of many-body condensed matter phenomena.

Our 1D lattice of magnetic microtraps is created by superimposing the magnetic field from a grooved, perpendicularly magnetized magnetic film with uniform bias fields B_{bx} and B_{by} along the x and y directions [Fig. 1(a)] [6,10]. The magnetic field components in the case of an infinite 1D lattice with no axial confinement along the x direction and for distances $z \gg a/2\pi$ from the magnetic microstructure are $[B_x, B_y, B_z] \approx [B_{bx}; B_0 \sin(ky)e^{-kz} + B_{by}; B_0 \cos(ky)e^{-kz}]$ [6], where a is the lattice period, $k = 2\pi/a$, $B_0 = 4M_z(e^{kt} - 1)$, t is the magnetic film thickness, and $4\pi M_z$ is the magnetization (in Gauss). A contour plot of calculated equipotentials, which are proportional to $|\mathbf{B}(x, y, z)|$, is shown in Fig. 1(a). The strength and direction of the bias fields determine the potential minima, their distance from the magnetic microstructure, the trap frequencies, and the barrier heights [6]. The potential minima need to be nonzero to prevent losses due to Majorana spin flips.

Details of the 1D $10\text{-}\mu\text{m}$ -period magnetic microstructure and atom chip are described elsewhere [10,30]. Briefly, the microstructure consists of a $10\ \text{mm} \times 10\ \text{mm}$ magnetic film deposited on a microfabricated grooved silicon substrate on the atom chip, which is mounted upside-down in the

*phannaford@swin.edu.au

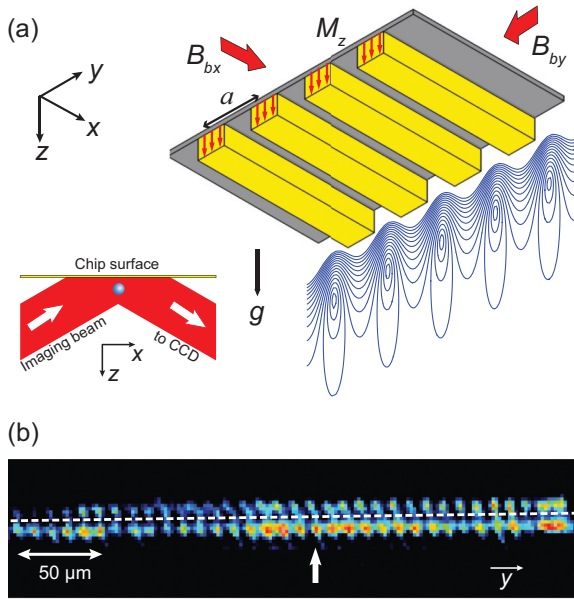


FIG. 1. (Color online) (a) Schematic of the magnetic microstructure used to create a periodic 1D lattice of magnetic microtraps with nonzero potential minima. Contour lines are equipotentials calculated for the parameters in this experiment with contour interval of 0.5 G. (b) Part of the absorption image for an array of clouds of ^{87}Rb $|F = 1, m_F = -1\rangle$ atoms trapped in the 1D 10- μm -period magnetic lattice, after evaporative cooling to a trap depth $\delta f = (f_f - f_0) = 100$ kHz, which cools the atoms below the critical temperature. The image was recorded using reflective absorption imaging along the axial x direction (see inset), which produces images both after reflection (bottom image) and prior to reflection (top image) of the imaging beam from the chip surface (dashed line). The effective pixel size is 2.0 μm . The vertical arrow indicates the lattice site (site 38) at which the rf spectra in Fig. 2 were recorded.

UHV chamber. The magnetic film is a six-layer structure of 1.0- μm -thick perpendicularly magnetized $\text{Tb}_6\text{Gd}_{10}\text{Fe}_{80}\text{Co}_4$ (total thickness 1.3 μm), for which $4\pi M_z \sim 3$ kG, $H_c \sim 6$ kOe, and $T_{\text{Curie}} \sim 300$ $^\circ\text{C}$ [31]. The magnetic microstructure is mounted 300 μm below a combined U and Z wire oriented with its central section perpendicular to the grooves. The bias fields and weak axial confinement are provided by the current-carrying Z wire [30]. For $I_z = 17$ A and $B_{bx} = 51$ G, the trap frequencies determined from numerical simulations are $\omega_x/2\pi = 259$ Hz and $\omega_{y,z}/2\pi = 7.3$ kHz, which is consistent with $\omega_y/2\pi = 7.5$ kHz measured by parametric heating. The trap frequencies correspond to a geometric mean frequency $\bar{\omega}/2\pi = (\omega_x\omega_y^2)^{1/3}/2\pi = 2.40$ kHz and an aspect ratio of 30. In comparison to earlier experiments on a 2D magnetic lattice [11], $\bar{\omega}$ is about four times smaller, and correspondingly, the expected three-body loss rates, which scale as $\bar{\omega}^6$ [32], are about 10^4 times smaller. The calculated barrier heights are $\Delta B_y = 4$ G (130 μK) and $\Delta B_z \sim 1$ G (30 μK).

Typically, 1×10^8 ^{87}Rb atoms are collected in a mirror magneto-optical trap (MOT) 1.2 mm below the chip before being transferred to a compressed U -wire MOT where they are polarization-gradient cooled and optically pumped to the $|F = 1, m_F = -1\rangle$ state. The atoms are then transferred to a Z -wire trap 600 μm below the chip where they are

evaporatively cooled. About 3×10^6 atoms at 10–15 μK are then brought close to the magnetic lattice by ramping I_z from 38 A down to 17 A in 100 ms with $B_{bx} = 51$ G. Under these conditions the Z -wire trap merges smoothly with the magnetic lattice microtraps located 8 μm below the chip, allowing $\sim 1 \times 10^6$ atoms to be loaded into the magnetic lattice [30].

The lifetime of the atoms in the magnetic lattice microtraps is ~ 12 s, which is sufficient for the atoms to be evaporatively cooled (for 1.5 s) by ramping an rf field from 7.0 MHz down to a final evaporation frequency f_f . A trap depth of $\delta f = (f_f - f_0) = 100$ kHz (where f_0 is the trap bottom) leaves $\sim 5 \times 10^4$ atoms trapped in ~ 100 lattice sites, or $\langle N \rangle \sim 500$ atoms per site, in the central region of the lattice.

Figure 1(b) shows part of an *in situ* absorption image for a periodic array of clouds of ^{87}Rb $|F = 1, m_F = -1\rangle$ atoms trapped in multiple sites of the 1D 10- μm -period magnetic lattice after evaporative cooling to a trap depth $\delta f = 100$ kHz, which cools the atoms below the critical temperature. The image was recorded using reflective absorption imaging [33] along the long axis of the elongated atom clouds. The imaging beam is focused by a cylindrical lens into a light sheet and sent at a slight angle ($\sim 2^\circ$) to the reflecting gold surface of the chip, resulting in images both after and prior to reflection. Detection of the two images provides a measure of the distance of the trapped atoms from the chip surface (8 μm). The effective pixel size is 2.0 μm , corresponding to 5.0 pixels per lattice period. The measured resolution from the width of the images of individual sites is 4 μm .

The clouds of atoms in Fig. 1(b) are resolved in their individual lattice sites, which allows us to perform site-resolved measurements. The variation in site-to-site transmitted intensity ($\sim \pm 30\%$) across the lattice is due mainly to imperfections in the gold mirror on the chip surface and to nonuniform loading of the lattice and nonuniformity of the imaging light. In addition, some of the variation is due to inhomogeneity in the magnetic lattice. The positions of the individual clouds of atoms reveal that the lattice period is constant to within 1% across the lattice.

Figure 2 presents *in situ* rf spectra of atom loss over a range of rf frequencies f taken at a single lattice site [site 38, vertical arrow in Fig. 1(b)] after the atoms have been evaporatively cooled to trap depths $\delta f = 600, 400,$ and 100 kHz. The power of the rf pulse was reduced to one-tenth of that used for evaporative cooling to minimize power broadening, and the rf pulse duration was 40 ms. The rf spectra evolve from (a) a broad truncated Boltzmann-type frequency distribution for $\delta f = 600$ kHz, characteristic of a thermal cloud, through to (c) a narrow Thomas-Fermi-type frequency distribution for $\delta f = 100$ kHz, characteristic of a BEC. For (b), $\delta f = 400$ kHz, the rf spectrum exhibits a pronounced bimodal distribution consisting of BEC plus thermal cloud components [34]. The critical temperature for quantum degeneracy for $N = 500$ atoms per site ($\delta f = 100$ kHz) and $\bar{\omega}/2\pi = 2.40$ kHz is $T_c = 0.9$ μK . The time decay of the BECs in the magnetic lattice corresponds to a half-life of ~ 0.5 s.

To fit the data in Fig. 2, we use a self-consistent mean-field model which takes account of atom-atom interactions in both the BEC and thermal cloud and the mutual interaction between them [11], but neglects the kinetic energy of the condensate fraction via the Thomas-Fermi approximation and effects of

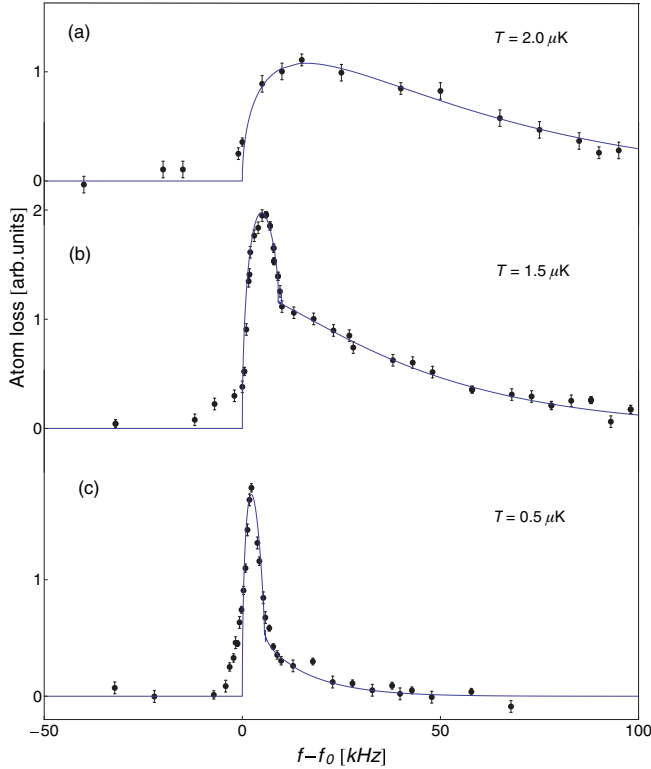


FIG. 2. (Color online) Rf spectra for ^{87}Rb $|F = 1, m_F = -1\rangle$ atoms after evaporative cooling in the 1D magnetic lattice to trap depths $\delta f = (f_f - f_0)$ of (a) 600 kHz, (b) 400 kHz, and (c) 100 kHz in lattice site 38. The solid lines represent fits to the data based on a self-consistent mean-field model for a BEC plus thermal cloud as described in the text.

gravity sag in the tightly confining magnetic traps. For the density distribution of the condensates we use [35]

$$n_c(r) = \text{Max} \left\{ \left(\frac{1}{g} \right) [\mu - V(r) - 2gn_{\text{th}}(r)]; 0 \right\}, \quad (1)$$

where $n_{\text{th}}(r) = \text{Li}_{3/2}[\exp(-|\mu - V_{\text{eff}}(r)|/k_B T)]/\lambda_{\text{dB}}^3$ is the density distribution of the thermal cloud, $V_{\text{eff}}(r) = V(r) + 2g[n_{\text{th}}(r) + n_c(r)]$, and $V(r) = 1/2M(\omega_x^2 x^2 + \omega_y^2 y^2 + \omega_z^2 z^2)$ is the confining harmonic potential. $\text{Li}_{3/2}[z]$ is the polylogarithmic function with base 3/2, λ_{dB} is the thermal de Broglie wavelength, $g = 4\pi\hbar^2 a_s/M$ is the mean-field coupling constant, M is the atom mass, and a_s is the s -wave scattering length. Equation (1) is solved iteratively to obtain $n_c(r)$ for a given temperature T and chemical potential μ , where the elongated cloud with trap frequencies ω_x and ω_y can be replaced by a spherical cloud with mean trap frequency $\bar{\omega} = (\omega_x \omega_y)^{1/3}$. The rf frequency distribution is then obtained from the resonance condition $hf = \mu_B |g_F B|$ for $\Delta m_F = \pm 1$ spin-flip transitions and by determining the number of atoms $\Delta N(f)$ in a spherical shell $4\pi r^2 \Delta r$ of constant frequency f that are removed by a rf knife of width Δf . For the case of a pure BEC, the number of trapped atoms removed by the rf knife at frequency f is $\Delta N(f) \propto \text{Max}\{f^{1/2}(\mu/(|m_F|h) - f)\Delta f; 0\}$ with a base width $\mu/(|m_F|h)$.

The solid lines in Fig. 2 represent fits to the rf spectra using the above model. For a given data set, μ and T are

TABLE I. Trap bottom (f_0), chemical potential (μ/h), atom temperature (T), condensate fraction (%), and atom number (N_{abs}) derived from absorption images and normalized to $\langle N_{\mu, T} \rangle$, for various sites across the lattice. The trap depth δf is 100 kHz.

Site	f_0 (MHz)	μ/h (kHz)	T (μK)	BEC (%)	N_{abs} (atoms)
22	4.9318 (5)	7.0 (1.0)	0.55 (5)	37 (5)	240 (100)
35	4.9320 (5)	7.5 (0.5)	0.50 (5)	50 (5)	510 (50)
36	4.9322 (5)	7.5 (0.5)	0.50 (5)	50 (5)	430 (50)
37	4.9323 (5)	7.7 (0.5)	0.58 (5)	39 (5)	430 (50)
38	4.9322 (5)	7.5 (0.5)	0.50 (5)	50 (5)	460 (50)
39	4.9322 (5)	7.3 (0.5)	0.52 (5)	45 (5)	490 (50)
40	4.9324 (5)	7.5 (0.5)	0.55 (5)	42 (5)	480 (50)
41	4.9324 (5)	7.0 (0.5)	0.55 (5)	37 (5)	370 (50)
42	4.9324 (5)	7.0 (0.5)	0.55 (5)	37 (5)	400 (50)
43	4.9320 (5)	8.0 (0.5)	0.60 (5)	39 (5)	320 (50)
44	4.9325 (5)	7.5 (0.5)	0.53 (5)	45 (5)	430 (50)
67	4.9320 (5)	7.8 (0.5)	0.60 (5)	38 (5)	440 (50)
70	4.9319 (5)	7.2 (0.5)	0.56 (5)	38 (5)	390 (50)
71	4.9320 (5)	7.8 (0.5)	0.55 (5)	45 (5)	460 (50)
85	4.9320 (5)	8.7 (1.0)	0.60 (5)	44 (5)	450 (100)

varied until the calculated rf spectrum provides a reasonable fit to the experimental spectrum with the constraint that the total atom number $N_{\mu, T}$ derived from μ and T is consistent with the atom number N_{abs} derived from the absorption image and normalized to $\langle N_{\mu, T} \rangle$ for various lattice sites. For the trap depth $\delta f = 400$ kHz [Fig. 2(b)], the data fit well to a narrow BEC component plus a broad thermal cloud component with chemical potential $\mu/h = 19$ kHz, corresponding to $N \sim 8700$ atoms, and temperature $T = 1.5$ μK . The slight rounding of the leading edge of the spectrum is attributed to residual power broadening. For the trap depth $\delta f = 100$ kHz [Fig. 2(c)], the fit yields $\mu/h = 7.5$ kHz, corresponding to $N \sim 380$ atoms, and $T = 0.50$ μK . The condensate fraction deduced from the fit is 50 (5)%, or 54 (5)% if we include the contribution from the rounded leading edge in Fig. 2(c).

Our absorption imaging scheme allows rf spectra to be recorded simultaneously for all of the ~ 100 populated sites across the magnetic lattice, with a total acquisition time of about 1 h. The spectrum for each of the analyzed lattice sites exhibits a strong BEC component, similar to Fig. 2(c). Table I summarizes the results for a sample of 15 sites which are representative of the central region (sites 23–85) of the lattice, including a string of ten adjacent sites (35–44), and sites near the ends of the central region. The site-to-site variations in f_0 , μ , T , and condensate fraction indicate that the sites are remarkably uniform across the lattice. In particular, the trap bottoms, which could be accurately determined from the intercepts of the fitted rf spectra with the $(f - f_0)$ axis, show site-to-site variations of only ± 0.4 kHz corresponding to ± 0.6 mG in 7.0 G. This degree of uniformity across the lattice is not reflected in the absorption image in Fig. 1(b) or in the atom numbers N_{abs} derived from the absorption image which show significant variations in transmitted intensity as discussed above.

As an independent check for the onset of Bose-Einstein condensation in the magnetic lattice we measure the atom loss rate due to three-body recombination. For a BEC, the

density-density fluctuations are suppressed relative to a thermal cloud, due to a factor of 6 smaller three-particle correlation function $g^{(3)}$ [28]. The three-body recombination loss rate is given by $dN(t)/dt = -K_3 \int n^3(\mathbf{r}, t) d^3r$, where K_3 is the loss rate constant. Assuming that during the atom loss the BEC maintains a Thomas-Fermi profile, the atom number decay becomes $N_c(t) = N_0(t)(1 + \beta t)^{-5/4}$ where $\beta = (32/105)K_3 n_{c,p}^2(0)$ and $n_{c,p}(0)$ is the initial peak density of the condensate. The three-body recombination rate is measured by monitoring the atom loss for hold times out to 500 ms where the condensate still persists. A power-law fit to the atom decay curve yields an exponent of $-1.21(4)$, which is consistent with the BEC value of $-5/4$ but significantly different from the thermal cloud value of $-1/2$. For an initial peak density $n_{c,p}(0) = 8 \times 10^{14} \text{ cm}^{-3}$, which was determined from analysis of the rf spectra, the three-body decay constant is found to be $K_3 = 5.5(1.0) \times 10^{-30} \text{ cm}^6 \text{ s}^{-1}$, which is consistent with previous measurements for ^{87}Rb ($F = 1, m_F = -1$) atoms [28,36], but much smaller than the value $K_3 = 4.2(1.8) \times 10^{-29} \text{ cm}^6 \text{ s}^{-1}$ measured for a thermal cloud [28].

Arrays of BECs in a $10\text{-}\mu\text{m}$ -period magnetic lattice are promising for the implementation of Rydberg-interacting quantum systems by exploiting the long-range dipolar interaction between atoms excited to Rydberg states. The size of each BEC in the array is well within the typical Rydberg blockade radius, so that each BEC could potentially be used as a collective qubit. The interaction driven level shift between two $n \approx 80$ s Rydberg excitations at a distance of $10 \mu\text{m}$ is still several MHz, which far exceeds the Rydberg state decay rate [22]. At the same time, each trap is sufficiently far from the chip surface to minimize unwanted surface effects [15]. It should also be possible to create spatially separated Rydberg-dressed BECs [21] or degenerate Fermi gases, in which Rydberg states are weakly admixed to the atoms, resulting in strong long-range and anisotropic interactions. This might enable the realization of “coupled quantum gases” where atoms in spatially separated traps may strongly influence one another (e.g., [37]).

Another application will be to engineer simple graphene-like model systems with tunable parameters, for example, using magnetic lattices with hexagonal symmetry loaded from a BEC or degenerate Fermi gas. In periodic lattices the tunneling rates scale with period a and barrier height V_0 as $J \propto a^{-1/2} V_0^{3/4} \exp[-C V_0^{1/2} a]$ [where $C = (32M)^{1/2}/h$] [1]. For a square optical lattice with $a = 0.64 \mu\text{m}$, the tunneling rate for ^{87}Rb atoms is estimated to be $J \sim 20 \text{ Hz}$ for $V_0 \sim 12E_r$ (where E_r is the recoil energy) [38] or $J \sim 330 \text{ Hz}$ for $V_0 \sim 6E_r$. Thus, in order to have significant tunneling rates in a magnetic lattice, submicron periods are required. Due to the tighter confinement, atomic states with low inelastic collision rates should be chosen (for example, fermionic atoms such as ^{40}K) or the number of atoms per site should be limited to less than three, which would normally be the case for a 2D lattice with submicron period. Additionally, the magnetic potentials need to be smooth and homogeneous with constant periodicity ($<1\% - 2\%$ [20]) and uniform trap bottoms. To produce high-quality magnetic potentials with submicron periods we propose to use nanofabricated multilayer Co/Pd (or Pt) films (with $\sim 6 \text{ nm}$ grain size) presently under development for high density data storage.

In conclusion, we have realized a periodic array of Bose-Einstein condensates in a $10\text{-}\mu\text{m}$ -period 1D magnetic lattice. A clear signature for the onset of BEC was provided by *in situ* site-resolved rf spectra which show a pronounced bimodal distribution. Similar bimodal distributions were found for various sites across the magnetic lattice. This result represents a major advance towards the implementation of magnetic lattices to create periodic arrays of BECs for quantum simulation of many-body condensed matter phenomena in lattices of complex geometry and arbitrary period.

We thank Mandip Singh, Brenton Hall, and Chris Vale for fruitful discussions. We acknowledge funding from an ARC Discovery Project grant (Grant No. DP130101160).

-
- [1] I. Bloch, J. Dalibard, and W. Zwerger, *Rev. Mod. Phys.* **80**, 885 (2008).
- [2] T. Kinoshita, T. Wenger, and D. S. Weiss, *Nature (London)* **440**, 900 (2006).
- [3] M. Takamoto, F.-L. Hong, R. Higashi, and H. Katori, *Nature (London)* **435**, 321 (2005).
- [4] T. Calarco, E. A. Hinds, D. Jaksch, J. Schmiedmayer, J. I. Cirac, and P. Zoller, *Phys. Rev. A* **61**, 022304 (2000).
- [5] C. Monroe, *Nature (London)* **416**, 469 (2007).
- [6] S. Ghanbari, T. D. Kieu, A. Sidorov, and P. Hannaford, *J. Phys. B* **39**, 847 (2006).
- [7] R. Gerritsma and R. J. C. Spreeuw, *Phys. Rev. A* **74**, 043405 (2006).
- [8] R. Gerritsma, S. Whitlock, T. Fernholz, H. Schlatter, J. A. Luigjes, J.-U. Thiele, J. B. Goedkoop, and R. J. C. Spreeuw, *Phys. Rev. A* **76**, 033408 (2007).
- [9] M. Boyd, E. W. Streed, P. Medley, G. K. Campbell, J. Mun, W. Ketterle, and D. E. Pritchard, *Phys. Rev. A* **76**, 043624 (2007).
- [10] M. Singh, M. Volk, A. Akulshin, A. Sidorov, R. McLean, and P. Hannaford, *J. Phys. B* **41**, 065301 (2008).
- [11] S. Whitlock, R. Gerritsma, T. Fernholz, and R. J. C. Spreeuw, *New J. Phys.* **11**, 023021 (2009).
- [12] R. Schmied, D. Leibfried, R. J. C. Spreeuw, and S. Whitlock, *New J. Phys.* **12**, 103029 (2010).
- [13] A. Abdelrahman, M. Vasiliev, K. Alameh, and P. Hannaford, *Phys. Rev. A* **82**, 012320 (2010).
- [14] I. Llorente Garcia, B. Darquie, E. A. Curtiss, C. D. J. Sinclair, and E. A. Hinds, *New J. Phys.* **12**, 093017 (2010).
- [15] V. Y. F. Leung, A. Tauschinsky, N. J. van Druten, and R. J. C. Spreeuw, *Quantum Inf. Process.* **10**, 955 (2011).
- [16] V. Y. F. Leung *et al.*, *Rev. Sci. Instrum.* **85**, 053102 (2014).
- [17] J. Yin, W. Gao, J. Hu, and Y. Wang, *Opt. Commun.* **206**, 99 (2002).
- [18] A. Grabowski and T. Pfau, *Eur. Phys. J. D* **22**, 347 (2003).
- [19] A. Günther, M. Kemmler, S. Kraft, C. J. Vale, C. Zimmermann, and J. Fortágh, *Phys. Rev. A* **71**, 063619 (2005).

- [20] O. Romero-Isart, C. Navau, A. Sanchez, P. Zoller, and J. I. Cirac, *Phys. Rev. Lett.* **111**, 145304 (2013).
- [21] J. Honer, H. Weimer, T. Pfau, and H. P. Büchler, *Phys. Rev. Lett.* **105**, 160404 (2010).
- [22] M. Saffman, T. G. Walker, and K. Mølmer, *Rev. Mod. Phys.* **82**, 2313 (2010).
- [23] M. Lewenstein, A. Sanpera, V. Ahufinger, B. Damski, A. Sen, and U. Sen, *Adv. Phys.* **56**, 243 (2007).
- [24] S.-L. Zhu, B. Wang, and L.-M. Duan, *Phys. Rev. Lett.* **98**, 260402 (2007).
- [25] L. Tarruell, D. Greif, T. Uehlinger, G. Jotzu, and T. Esslinger, *Nature (London)* **483**, 302 (2012).
- [26] T. Uehlinger, G. Jotzu, M. Messer, D. Greif, W. Hofstetter, U. Bissbort, and T. Esslinger, *Phys. Rev. Lett.* **111**, 185307 (2013).
- [27] S. Whitlock, B. V. Hall, T. Roach, R. Anderson, M. Volk, P. Hannaford, and A. I. Sidorov, *Phys. Rev. A* **75**, 043602 (2007).
- [28] E. A. Burt, R. W. Ghrist, C. J. Myatt, M. J. Holland, E. A. Cornell, and C. E. Wieman, *Phys. Rev. Lett.* **79**, 337 (1997).
- [29] J. Soeding, D. Guery-Odelin, P. Desbiolles, F. Chevy, H. Inamori, and J. Dalibard, *Appl. Phys. B* **69**, 257 (1999).
- [30] S. Jose, Ph.D. thesis, Swinburne University, 2013.
- [31] J. Y. Wang, S. Whitlock, F. Scharnberg, D. S Gough, A. I. Sidorov, R. J. McLean, and P. Hannaford, *J. Phys. D* **38**, 4015 (2005).
- [32] S. Whitlock, C. F. Ockeloen, and R. J. C. Spreeuw, *Phys. Rev. Lett.* **104**, 120402 (2010).
- [33] J. Armijo, T. Jacqumin, K. V. Kheruntsyan, and I. Bouchoule, *Phys. Rev. Lett.* **105**, 230402 (2010).
- [34] T. Fernholz, R. Gerritsma, S. Whitlock, I. Barb, and R. J. C. Spreeuw, *Phys. Rev. A* **77**, 033409 (2008).
- [35] F. Gerbier, J. H. Thywissen, S. Richard, M. Hugbart, P. Bouyer, and A. Aspect, *Phys. Rev. A* **70**, 013607 (2004).
- [36] B. Laburthe Tolra, K. M. O'Hara, J. H. Huckans, W. D. Phillips, S. L. Rolston, and J. V. Porto, *Phys. Rev. Lett.* **92**, 190401 (2004).
- [37] K. Lakomy, R. Nath, and L. Santos, *Phys. Rev. A* **85**, 033618 (2012).
- [38] W. S. Bakr, J. I. Gillen, A. Peng, S. Fölling, and M. Greiner, *Nature (London)* **462**, 74 (2009).